

Quantification of toxic metals using machine learning techniques and spark emission spectroscopy

Seyyed Ali Davari^{1,*} and Anthony S. Wexler^{1,2}

¹Air Quality Research Center (AQRC), University of California, Davis, 95616, Davis, USA

²Department of Mechanical and Aerospace Engineering, Civil and Environmental Engineering, and Land, Air and Water Resources, University of California, Davis, USA

Abstract

The United States Environmental Protection Agency (US EPA) list of Hazardous Air Pollutants (HAPs) includes toxic metal suspected or associated with development of cancer. Traditional techniques for detecting and quantifying toxic metals in the atmosphere are either not real time, hindering identification of sources, or limited by instrument costs. Spark emission spectroscopy is a promising and cost effective technique that can be used for analyzing toxic metals in real time. Here, we have developed a cost-effective spark emission spectroscopy system to quantify the concentration of toxic metals targeted by US EPA. Specifically, Cr, Cu, Ni, and Pb solutions were diluted and deposited on the ground electrode of the spark emission system. Least Absolute Shrinkage and Selection Operator (LASSO) was optimized and employed to detect useful features from the spark-generated plasma emissions. The optimized model was able to detect atomic emission lines along with other features to build a regression model that predicts the concentration of toxic metals from the observed spectra. The limits of detections (LOD) were estimated using the detected features and compared to the traditional single-feature approach. LASSO is capable of detecting highly sensitive features in the input spectrum; however for some toxic metals the single-feature LOD marginally outperforms LASSO LOD. The combination of low cost instruments with advanced machine learning techniques for data analysis could pave the path forward for data driven solutions to costly measurements.

1 Introduction

The United States Environmental Protection Agency (US EPA) lists a number of metals in their list of Hazardous Air Pollutants (HAPs). These metals are known or suspected to cause cancer or other serious health effects (Buzea et al. (2007); Pope III et al. (2002)). Table 1 lists the metals in US EPA’s HAPs list.

Table 2 lists other metals that are not on US EPA’s HAPs list but have been implicated in a range of

Table 1: List of hazardous metals targeted by US EPA

US EPA Metal HAPS
Antimony
Arsenic
Beryllium
Cadmium
Chromium
Cobalt
Lead
Manganese
Mercury
Nickel
Selenium

Table 2: List of other toxic metals

Toxic Metals
Copper
Iron
Zinc

adverse health effects so are of concern to the California Air Resources Board (CARB). It has been shown that presence of these metals are associated with various health concerns such as diabetes (Zanobetti et al. (2009)), cardiovascular disease (Brook et al. (2004)), and asthma (Gent et al. (2009)). Therefore, it is necessary to monitor and quantify their ambient concentration.

Various techniques over the years have been developed and used to measure metal particles. X-ray fluorescence (XRF) (Van Meel et al. (2007); Vincze et al. (2002)) and inductively coupled plasma mass spectrometry (ICP-MS) (Rovelli et al. (2018); Venecek et al. (2016)) have been used traditionally to quantify metals in atmospheric particles. XRF is excellent for measuring lighter elements and metals on filter substrates, but for field application it is expensive, has a high limit of detection (LOD) for heavier elements, and includes radiation risk. ICP-MS requires collection of aerosol on a substrate, such as a filter or impactor foil, extraction of the metals or elements from the substrate using harsh acidic chemicals, and then analyzing in the ICP-MS along with standards that help the instrument quantitate. Moreover, ICP-MS is most suitable for heavier elements and metals so has a high LOD for lighter toxic metals and is not available in field-deployed, real-time applications. Additionally, these instruments are expensive and hence are limited by cost and complexity as well.

Spark-induced breakdown spectroscopy (SIBS) and laser-induced breakdown spectroscopy (LIBS) have been employed in various applications from combustion (Do and Carter (2013); Kiefer et al. (2012); Kotzagianni et al. (2016)), nanomaterials (Davari et al. (2017a); De Giacomo et al. (2011); Hu et al. (2017); Matsumoto et al. (2015a,b, 2016)), and environmental/bio-hazards (Diwakar et al. (2012); Diwakar and Kulkarni (2012); Zheng et al. (2018b)), forensics (Martin et al. (2007)), semiconductors and thin films (Axente et al. (2014); Davari et al. (2017b, 2019); Hermann et al. (2019)), explosives (Gottfried et al. (2009)), pharmaceuticals (Mukherjee and Cheng (2008a,b); St-Onge et al. (2002)), and biomedical (Abbasi et al. (2018); Baudelet et al. (2006); Davari et al. (2018)). Particularly, Fisher et al. (2001) studied various toxic metals in aerosols by optimizing the spectrometer response with respect to gate delay. Hunter et al. (2000)

53 employed spark emission spectroscopy for continuous monitoring of metallic elements in aerosols. Yao et al.
54 (2018) used spark emission spectroscopy to obtain the carbon content of fly ashes. Diwakar and Kulkarni
55 (2012) employed spark emission spectroscopy coupled with a corona aerosol microconcentrator (CAM) to
56 improve the particle collection efficiency and detection limits of toxic metals. Zheng et al. (2017) character-
57 ized the CAM performance with respect to different experimental parameters and obtained the optimized
58 design parameters for their CAM system.

59 Recently, machine learning and deep learning techniques have been applied in different fields. These
60 techniques in general learn patterns that can be used to distinguish different labels. Boucher et al. (2015)
61 employed various linear and nonlinear machine learning techniques on LIBS spectra obtained from geological
62 samples and concluded that a combination of models yields a lower total error of prediction. Chengxu et al.
63 (2018) used convolutional neural networks to detect potassium in LIBS spectra and improve the linearity
64 of their prediction model incorporating deep convolutional layers. Zheng et al. (2018a) employed spark
65 emission spectroscopy on metals and used partial least squares regression to analyze their spectra set. They
66 compared their multivariate models to univariate models and showed in their study these two groups have
67 similar performance.

68 While LIBS and SIBS address issues regarding the field measurement and instrument complexity, they
69 are still considered expensive. Current interest in low-cost sensors and their ability to characterize local
70 air pollution concentrations motivated development of a low-cost system. We employed two complementary
71 approaches: (1) decreasing the cost of the electronics associated with SIBS and (2) incorporating advanced
72 data analysis techniques to improve quantification and limit of detection. In recent years, numerous studies
73 have used artificial neural networks (Ferreira et al. (2008)), partial least squares regression and least absolute
74 shrinkage and selection operator (LASSO) (Dyar et al. (2012)) on emission spectra to improve the quantifi-
75 cation and limit of detection of spectroscopic systems. In this study, we have developed a low-cost spark
76 emission spectroscopy system to quantify toxic metals. To reduce the overall cost, inexpensive replacements
77 for necessary components, such as the spark generator and delay generator have been developed in the lab.
78 To improve performance, advanced machine learning tools such as K-Means clustering and LASSO have
79 been employed to improve the system performance. The resulting instrument was evaluated against four
80 toxic metals listed by US EPA.

81 **2 Instrument development:**

82 **2.1 Spark generation system:**

83 Setting up a spark emission spectroscopy system requires expensive components. However, depending on
84 the application some of the components can be replaced. Components such as spark generator and delay
85 generator can cost up to \$10K and \$5K respectively. According to our application and needs, we developed
86 these components for less than \$600 and \$50 respectively. One costly component that is required for devel-
87 oping a spark emission spectroscopy system is the spark generation system. Numerous papers have studied
88 the fundamental principles of spark emission spectroscopy (Sacks and Walters (1970); Walters (1969, 1977)).
89 The key idea is to discharge a capacitor as quickly as possible to increase the power dissipated in the spark
90 gap. Fig. 1 illustrates the schematic of the spark generation system. The overall goal is to charge a capacitor
91 at high voltage and once it has been charged sufficiently, discharge the capacitor through the spark gap.
92 An Arduino board controls the timing between charging and discharging the capacitor. A boost convertor
93 converts 24v DC to 5000v DC and is connected to a mechanical relay with two switching states controlled
94 with the Arduino board. In the charge state, the mechanical relay provides the conduction path between
95 the boost convertor and the capacitor. In this configuration, the capacitor reaches full charge in 5s. Once
96 the capacitor is fully charged, the Arduino board sends a signal to turn off the boost convertor and sends
97 another signal to the mechanical relay to flip to the discharge state. At the discharge state, the mechanical
98 relay provides a conduction path between the capacitor and the spark gap. Shepherd et al. (2000) showed
99 that the discharge process could be controlled by a resistor after the spark gap. For low resistor values, the
100 spark current exhibited a periodic behavior as the capacitor discharges, which can be associated with an
101 under damped discharging. On the other hand, increasing the resistor value damped the discharge process
102 and dissipated a large portion of the capacitor energy through the resistor instead of the spark gap. We found
103 that 10 Ω resistor maximizes the power dissipation in the spark gap, while minimizing oscillations. Fig. 2

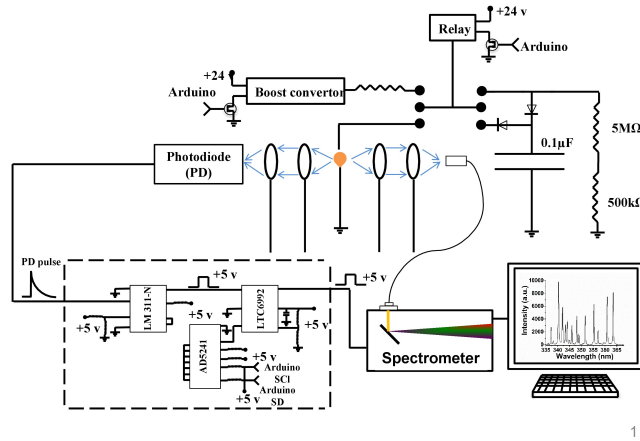


Figure 1: Schematic of the developed spark emission spectroscopy.

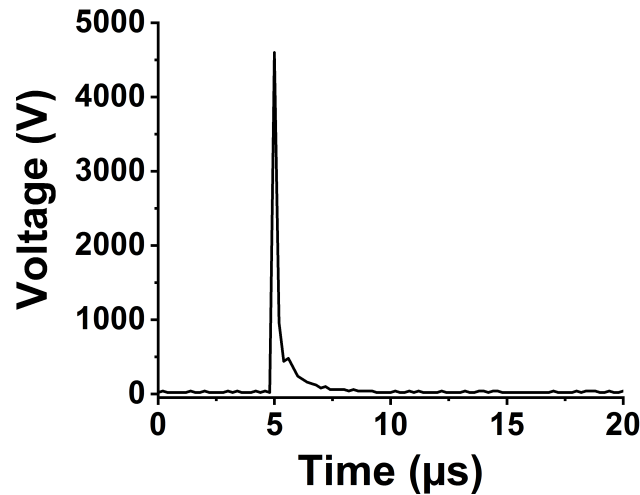


Figure 2: Spark voltage evolution in time.

104 illustrates the evolution of the generated spark as a function of time. The voltage shows a sudden increase
 105 followed by an exponential decrease fully discharging in less than $5\mu s$ and thus delivering sufficient energy
 106 to the arc and deposited analyte.

107 2.2 Delay generator:

108 The delay generator is another costly component typically used in time-resolved spectroscopy. Electronics
 109 advances have paved the way for developing a cost-effective delay generator. The delay generator suppresses
 110 initial noise in the emission spectrum so needs to cover a range between $1\mu s$ and $20\mu s$ with resolution less
 111 than $0.2\mu s$. We designed a custom-built delay generator in order to lower the overall cost of the instrument.
 112 Fig. 3 illustrates the schematic of the circuit. Upon generation of the spark-induced plasma, a pair of
 113 lenses collects and focuses the plasma emission into a photodiode. The pulse generated by the photodiode
 114 is passed into a voltage comparator (LM 311-N) to generate a transistor–transistor logic (TTL) signal. The
 115 output TTL signal from the comparator is sent to a pulse width modulator (PWM) controller (LTC6992),
 116 which adds delay to the TTL signal. An Arduino board adjusts a digital resistor (AD5241), which in turn
 117 determines the delay value. Fig. 4 shows the delay generator performance. The Y axis illustrates the delay
 118 values requested of the delay generator while the X axis shows the measured values. The red dashed line

119 shows the desired 1:1 line while the circles show the measured performance. The performance is linear over
 120 the relevant delay range with only a slight deviation from the 1:1 line. Considering the spark generated

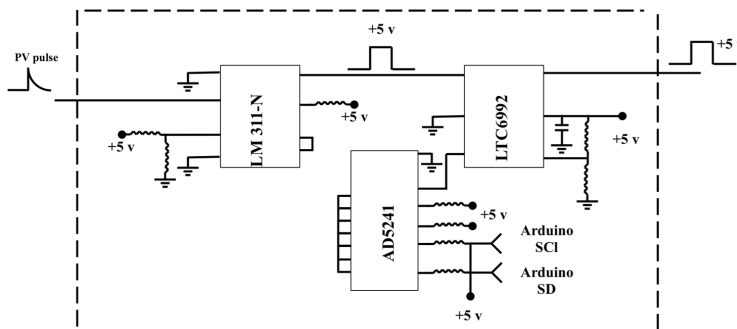


Figure 3: Schematic of the built-in delay generator.

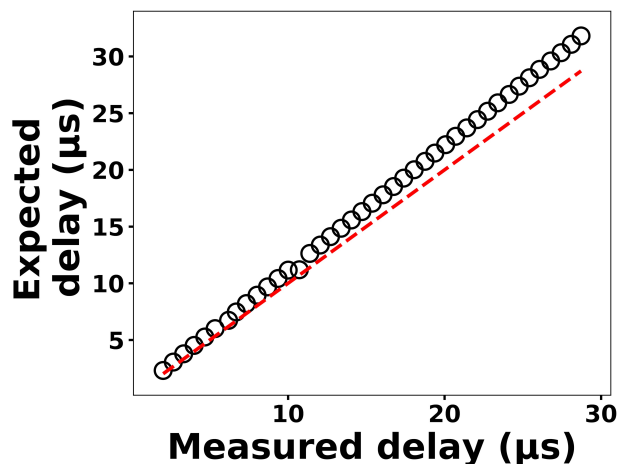


Figure 4: The expected delay set by the Arduino board as a function of the measured delay.

120 plasma short lifetime, our measurements require short delay values ($< 5\mu s$) where the built-in delay generator
 121 shows excellent performance and accuracy.
 122

123 2.3 Spectra Collection:

124 Four toxic metals with different concentrations were used to test the developed spark emission spectrometer
 125 system performance. Cr, Cu, Ni and Pd ($1000\mu g/mL$) were purchased from AccuStandard and diluted to
 126 specific concentrations. For each concentration more than 10 spectra have been collected and used for model
 127 development. A micropipette was used to deposit diluted solutions on a 1 mm diameter Tungsten ground
 128 electrode of the spark system for emission analysis. The total mass can be calculated from the deposited
 129 volume and solution concentration. Upon evaporation of the droplets, the capacitor was discharged to ablate
 130 the deposited material and obtain spectra. A pair of lenses (75mm focal length and 1" diameter, Thorlab)
 131 focused the emission into an optical fiber connected to a spectrometer (Ocean Optics).

132 3 Results and discussions:

133 To address shot-to-shot variations in the spark-generated plasma and nullify possible faults caused by the low
 134 cost components, an unsupervised learning technique, K-Means clustering, classifies the collected spectra.
 135 Following this procedure, it is possible to identify and remove outliers and hence improve the accuracy of

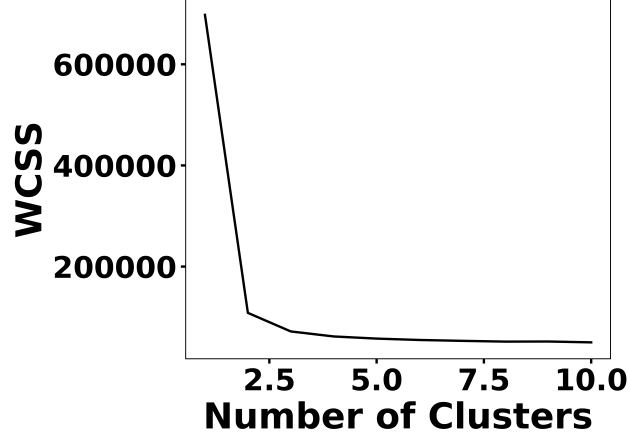


Figure 5: The elbow plot suggests two centroids for clustering the spectra set.

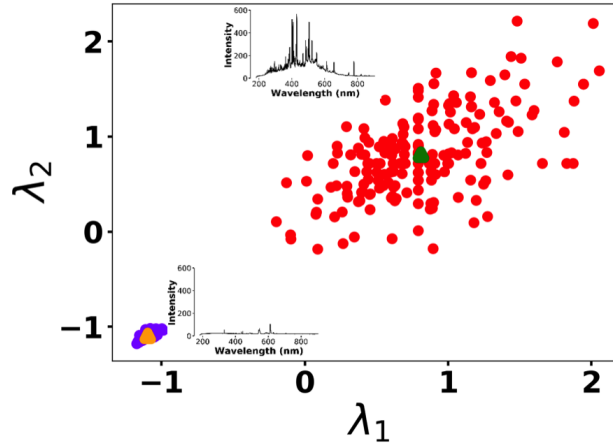


Figure 6: K-Means clustering for detecting outliers before passing the spectra set to LASSO model. Two clusters were plotted for the normalized intensities of two arbitrary wavelengths at λ_1 (208.365 nm) and λ_2 (208.759 nm).

136 the analysis. Fig. 5 illustrates the elbow plot that is used to optimize the number of spectral classes. The
 137 standard approach is to set the optimum number of clusters to the value where the within-cluster sum
 138 of squares (WCSS) error plateaus. The WCSS error plateaus once we have two or more centroids and
 139 therefore, the number of centroids is set to two. Fig. 6 illustrates the performance of the model for 300
 140 spectra obtained from the background (Tungsten ground electrode ablation). The results show clearly two
 141 clusters with different emission response. The lower left cluster containing $< 10\%$ of the spectra represent
 142 low-signal outliers so were eliminated from further analysis. For each toxic metal, 0.1, 1, 10 and 100 ng of
 143 mass were deposited on the ground electrode. For each concentration, 10 spectra were collected using $2 \mu\text{s}$
 144 delay between the observed and recorded emissions. After ablating the deposited mass and recording the
 145 spectrum, feature scaling has been used as a preprocessing step to improve the optimization process for out
 146 machine learning model. Plasma temperature can be obtained as:

$$I_{em} = \frac{hc}{\lambda_{ki}} N_k A_{ki} \quad (1)$$

$$N_k = N \frac{g_k e^{-\frac{E_k}{k_B T}}}{U(T)} \quad (2)$$

148 Combining equations (1) and (2) and taking log from both sides:

$$\ln\left(\frac{I_{em}\lambda_{ki}}{g_k A_{ki}}\right) = -\frac{E_k}{k_B T} + \ln\left(\frac{hcN}{U(T)}\right) \quad (3)$$

149 where k_B is Boltzmann constant, A_{ki} is the transition probability between two energy states (i) and (k), N_k
 150 is the population density at energy state k (E_k). λ_{ki} indicates the wavelength associated with the transition
 151 and g_k represents the degeneracy of energy state k. The slope of equation (3) is used to estimate the plasma
 152 temperature based on a series of Tungsten lines for the recorded cleaned spectra set at $2\mu s$. Fig. 7 illustrates
 153 the Boltzmann plot (Hahn and Omenetto (2010, 2012)) constructed by Tungsten lines. Based on the slope
 of the fit, the plasma temperature is estimated as 4013 ± 579 K. Upon identifying and removing the outlier

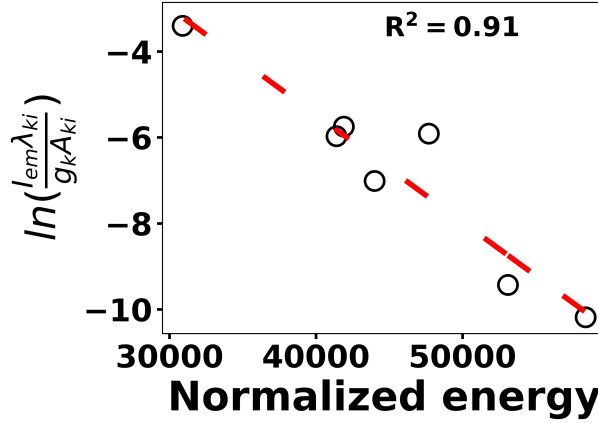


Figure 7: Boltzmann plot for various Tungsten lines in order to estimate plasma temperature.

154 spectra, the cleaned spectra set is normalized using the Tungsten peak at W I (400.87 nm) and fed into the
 155 Least Absolute Shrinkage and Selection Operator (LASSO) algorithm for model development and prediction.
 156

157 LASSO:

158 The cleaned scaled spectra set has been used to detect and quantify concentrations of the toxic metals.
 159 Simple linear regression obtains the slope and intercept of a linear line by minimizing the mean squared
 160 error between the predictions and known values. Least absolute shrinkage and selection operator (LASSO)
 161 detects and employs more features to perform predictions by optimizing the following loss function:

$$J(\theta) = \frac{1}{m} \sum_{i=1}^m (y^{(i)} - h_{\theta}(\mathbf{x}^{(i)}))^2 + c \sum_{j=1}^k |\theta_j| \quad (4)$$

162 where $\mathbf{x}^{(i)} \in \mathbb{R}^{2048}$ and $h_{\theta}(\mathbf{x}^{(i)})$ represent the normalized spectrum and the LASSO concentration prediction
 163 based on spectrum (i) ($\mathbf{x}^{(i)}$), respectively, and where $y^{(i)}$ is the known concentration corresponding to
 164 spectrum (i). m refers to total number of spectra and the LASSO coefficients are indicated by θ_j . k
 165 indicates the total number of features (spectral lines) used to build the model. The first term in equation
 166 (4) is the mean squared error and is common with simple linear regression, while the second term is a
 167 regularization term that minimizes the magnitude of θ_j . The L1 norm essentially sets most of the features
 168 in the spectrum to zero and maintains only a few features to build the linear model and perform predictions.
 169 The regularization constant (c) determines the number of features to be used in the model, and therefore
 170 the model loss needs to be optimized with respect to the regularization constant. To obtain the optimized
 171 regularization constant, we plotted the loss values for the Ni spectra training and testing sets as a function of
 172 number of features for various c values based on Leave-One-Out cross validation (Fig. 8). As expected, the
 173 train loss monotonically decreases as the number of features increases, while the loss for the test set initially

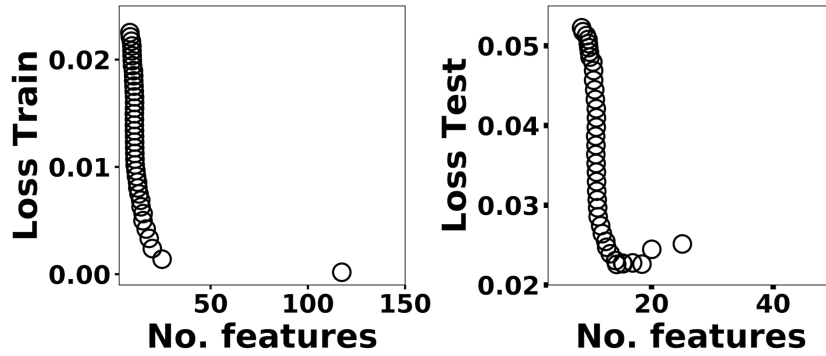


Figure 8: The train and test losses for Ni as a function of number of features.

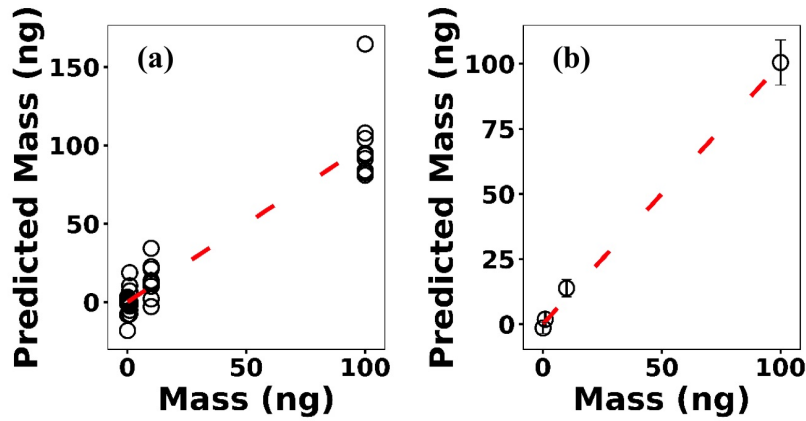


Figure 9: (a) LASSO predictions based on Leave-One-Out cross validation for Ni , (b) the averaged predictions for each concentration.

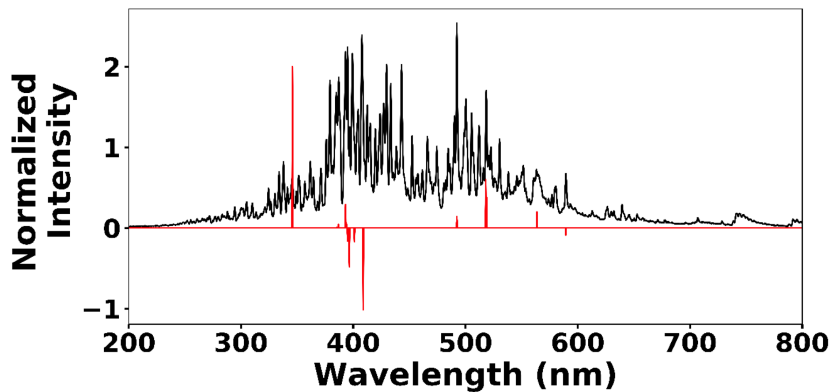


Figure 10: Ni 10ng spectrum (black line) and selected features by LASSO (red line).

174 decreases and then starts increasing. This implies that after incorporating a certain number of features into
 175 the model, the model starts memorizing rather than generalizing, which is known as overfitting. Therefore,
 176 we set the regularization constant to the value that minimizes the loss for the test set. Fig. 9 illustrates
 177 the optimized LASSO model predictions obtained by cross validation. For each concentration, the cross
 178 validation predictions were averaged and plotted along with the standard deviations. The predicted values
 179 vary linearly with the actuals. Figure 10 shows the wavelengths chosen by LASSO and the mean spectrum
 180 for 10 ng. LASSO chose a few Ni emission peaks along with other features to build the model. The same
 181 optimization process was applied to other toxic metals specifically Cr, Cu, and Pb. Fig. 11 illustrates the

resulting predictions and demonstrates the value of LASSO for predicting deposited mass from the spectra.

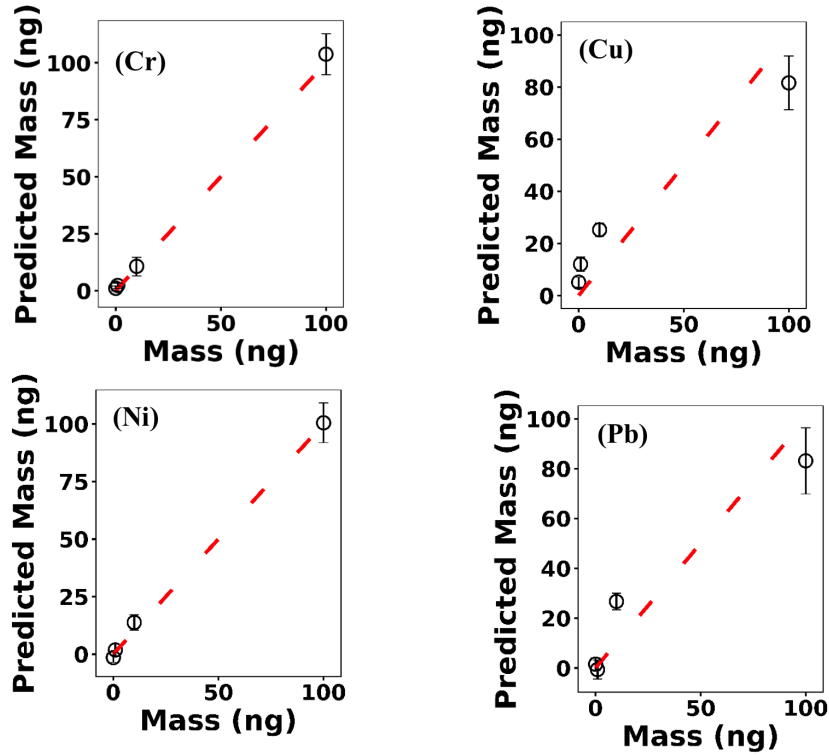


Figure 11: The optimized LASSO models predictions for Cr, Cu, Ni and Pb.

182

183

To obtain the limit of detection (LOD), the following function of the LASSO coefficients θ_j was used:

$$LOD = 3 \frac{\sigma_B}{S} = 3\sigma_B \|\theta_B\| \quad (5)$$

184

185

where σ_B is the standard deviation of the background and $\|\theta_B\|$ is the Euclidean norm of LASSO coefficients. Table 3 reports the LODs of the studied toxic metals.

Multivariate regression models such as LASSO might be more powerful in detection and quantification

Table 3: Detection limits for various toxic metals based on the LASSO and univariate models.

Toxic Metal	LASSO	R^2	MAE_{LASSO}	Univariate	R^2	$MAE_{Univariate}$	Regularization cons.
Cr	3.55	0.99	6.71	3.28	0.98	3.83	0.0008
Cu	12.09	0.92	49.67	0.68	0.11	143.27	0.0006
Ni	9.60	0.98	6.67	2.32	0.88	68.63	0.0009
Pb	54.40	0.90	36.67	8.37	0.45	124.42	0.0018

186

187

188

189

190

191

192

193

over univariate models; however, there is no guarantee that multivariate models outperform simple linear regression (Braga et al. (2010); Castro and Pereira-Filho (2016)). To evaluate LASSO performance, we compared LASSO with univariate methods, by calculating the LODs using simple univariate linear regression based on the features selected by LASSO. Fig. 12 illustrates the LODs obtained using this univariate technique (circles) compared to LASSO LOD (dashed line) for Ni. Considering only the sensitivity (LOD) is necessary but not sufficient for evaluating model performance since low R^2 values are also problematic. Therefore, in order to incorporate both R^2 and LOD for model assessment, we defined a score as:

$$Score = \left(\frac{LOD}{R^2}\right)^2 \quad (6)$$

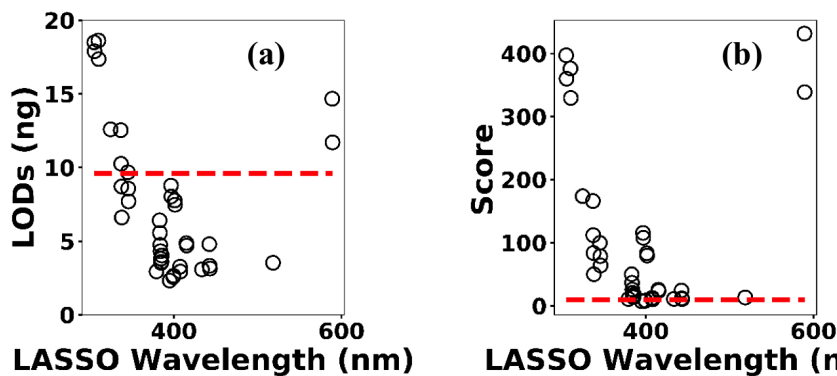


Figure 12: (a) the univariate LODs based on LASSO selected features and (b) LASSO and univariate models scores.

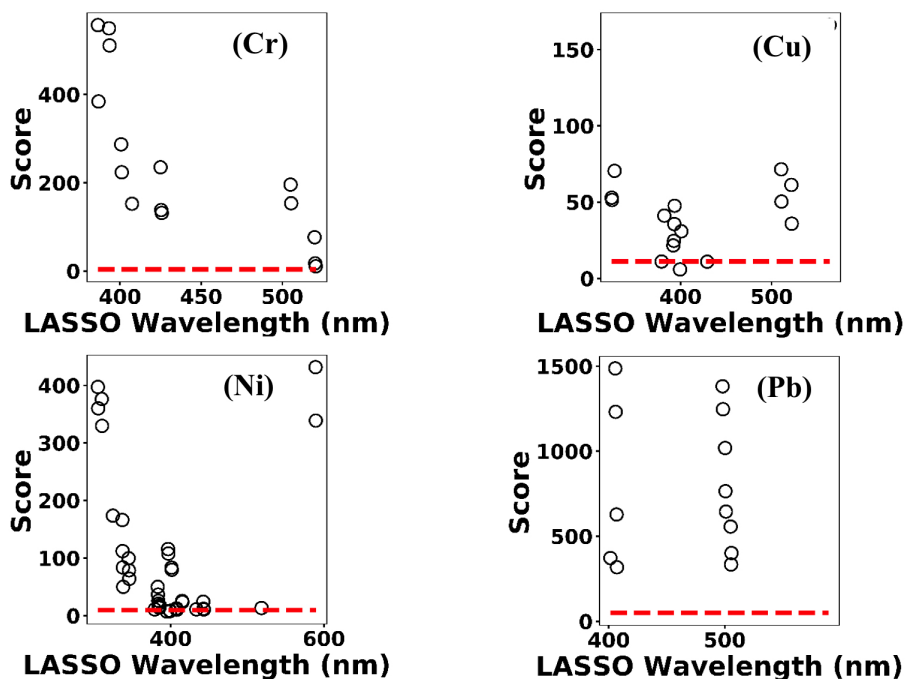


Figure 13: Model scores defined by equation 3 for Cr, Cu, Ni and Pb. Circles indicate univariate models scores and dashed lines correspond to LASSO scores.

194 Based on this definition, a model that has low LOD and high R^2 is desirable. LASSO score outperforms
 195 single feature linear regression for Pb, but the two methods were comparable for Cu, Ni, and Cr (Fig. 13).
 196 Other studies have reported that univariate techniques performed better than multivariate ones (Braga et al.
 197 (2010); Castro and Pereira-Filho (2016)). In LASSO, this may be related to the cost function defined for
 198 the regression (equation (4)). LASSO is a special case of elastic net family where both L1 and L2 norms
 199 are combined and used in the cost function. Considering the cost function in equation (4), the model goal is
 200 to minimize the prediction error and coefficient values (minimizing L1). This does not necessarily optimize
 201 LOD. Therefore, cost function minimization does not correspond to LOD minimization. Considering Fig.
 202 12, using features defined by LASSO in a univariate model may yield better LOD than that obtained by
 203 LASSO alone. This might be an advantageous approach if the physical intuition of the features is not as
 204 important as detection of toxic metals.

205 **4 Conclusion**

206 A cost-effective spark emission spectroscopy instrument was designed and developed to quantify toxic metals
207 targeted by US EPA and the California Air Resources Board. Costly components such as the spark generation
208 system and delay generator were developed to lower the overall cost. An unsupervised learning technique
209 was employed to detect outlier spectra. The cleaned spectra set was fed into LASSO for predicting the
210 concentration of deposited samples on the ground electrode of the spark system from spectra obtained
211 from the plasma. A combination of LASSO feature detection with univariate regression might improve the
212 detection limits. Our results illustrate the promising realm of cost-effective sensors combined with advanced
213 machine-learning techniques to provide data driven solutions to the traditional challenging problems.

214 **Funding**

215 California Air Resources Board (CARB).

216 **Disclosures**

217 The authors declare no conflicts of interest.

218 References

- 219 Abbasi, H., Rauter, G., Guzman, R., Cattin, P. C., and Zam, A.: Laser-induced breakdown spectroscopy
220 as a potential tool for autocarbonization detection in laserosteotomy, *Journal of biomedical optics*, 23,
221 071 206, 2018.
- 222 Axente, E., Hermann, J., Socol, G., Mercadier, L., Beldjilali, S. A., Cirisan, M., Luculescu, C. R., Ristoscu,
223 C., Mihailescu, I. N., and Craciun, V.: Accurate analysis of indium–zinc oxide thin films via laser-induced
224 breakdown spectroscopy based on plasma modeling, *Journal of Analytical Atomic Spectrometry*, 29, 553–
225 564, 2014.
- 226 Baudalet, M., Guyon, L., Yu, J., Wolf, J.-P., Amodeo, T., Fréjafon, E., and Laloi, P.: Femtosecond time-
227 resolved laser-induced breakdown spectroscopy for detection and identification of bacteria: A comparison
228 to the nanosecond regime, *Journal of Applied Physics*, 99, 084 701, 2006.
- 229 Boucher, T. F., Ozanne, M. V., Carmosino, M. L., Dyar, M. D., Mahadevan, S., Breves, E. A., Lepore,
230 K. H., and Clegg, S. M.: A study of machine learning regression methods for major elemental analysis
231 of rocks using laser-induced breakdown spectroscopy, *Spectrochimica Acta Part B: Atomic Spectroscopy*,
232 107, 1–10, 2015.
- 233 Braga, J. W. B., Trevizan, L. C., Nunes, L. C., Rufini, I. A., Santos Jr, D., and Krug, F. J.: Comparison of
234 univariate and multivariate calibration for the determination of micronutrients in pellets of plant materials
235 by laser induced breakdown spectrometry, *Spectrochimica Acta Part B: Atomic Spectroscopy*, 65, 66–74,
236 2010.
- 237 Brook, R. D., Franklin, B., Cascio, W., Hong, Y., Howard, G., Lipsett, M., Luepker, R., Mittleman, M.,
238 Samet, J., Smith Jr, S. C., et al.: Air pollution and cardiovascular disease: a statement for healthcare pro-
239 fessionals from the Expert Panel on Population and Prevention Science of the American Heart Association,
240 *Circulation*, 109, 2655–2671, 2004.
- 241 Buzea, C., Pacheco, I. I., and Robbie, K.: Nanomaterials and nanoparticles: sources and toxicity, *Biointer-
242 phases*, 2, MR17–MR71, 2007.
- 243 Castro, J. P. and Pereira-Filho, E. R.: Twelve different types of data normalization for the proposition
244 of classification, univariate and multivariate regression models for the direct analyses of alloys by laser-
245 induced breakdown spectroscopy (LIBS), *Journal of Analytical Atomic Spectrometry*, 31, 2005–2014, 2016.
- 246 Chengxu, L., Bo, W., Jiang, X., Zhang, J., Kang, N., and Yanwei, Y.: Detection of K in soil using time-
247 resolved laser-induced breakdown spectroscopy based on convolutional neural networks, *Plasma Science
248 and Technology*, 21, 034 014, 2018.
- 249 Davari, S. A., Hu, S., and Mukherjee, D.: Calibration-free quantitative analysis of elemental ratios in inter-
250 metallic nanoalloys and nanocomposites using Laser Induced Breakdown Spectroscopy (LIBS), *Talanta*,
251 164, 330–340, 2017a.
- 252 Davari, S. A., Hu, S., Pamu, R., and Mukherjee, D.: Calibration-free quantitative analysis of thin-film
253 oxide layers in semiconductors using laser induced breakdown spectroscopy (LIBS), *Journal of Analytical
254 Atomic Spectrometry*, 32, 1378–1387, 2017b.
- 255 Davari, S. A., Masjedi, S., Ferdous, Z., and Mukherjee, D.: In-vitro analysis of early calcification in aortic
256 valvular interstitial cells using Laser-Induced Breakdown Spectroscopy (LIBS), *Journal of biophotonics*,
257 11, e201600 288, 2018.
- 258 Davari, S. A., Taylor, P. A., Standley, R. W., and Mukherjee, D.: Detection of interstitial oxygen contents
259 in Czochralski grown silicon crystals using internal calibration in laser-induced breakdown spectroscopy
260 (LIBS), *Talanta*, 193, 192–198, 2019.

- 261 De Giacomo, A., De Bonis, A., Dell'Aglio, M., De Pascale, O., Gaudio, R., Orlando, S., Santagata, A.,
262 Senesi, G., Taccogna, F., and Teghil, R.: Laser ablation of graphite in water in a range of pressure from
263 1 to 146 atm using single and double pulse techniques for the production of carbon nanostructures, *The*
264 *Journal of Physical Chemistry C*, 115, 5123–5130, 2011.
- 265 Diwakar, P., Kulkarni, P., and Birch, M. E.: New approach for near-real-time measurement of elemental
266 composition of aerosol using laser-induced breakdown spectroscopy, *Aerosol Science and Technology*, 46,
267 316–332, 2012.
- 268 Diwakar, P. K. and Kulkarni, P.: Measurement of elemental concentration of aerosols using spark emission
269 spectroscopy, *Journal of analytical atomic spectrometry*, 27, 1101–1109, 2012.
- 270 Do, H. and Carter, C.: Hydrocarbon fuel concentration measurement in reacting flows using short-gated
271 emission spectra of laser induced plasma, *Combustion and Flame*, 160, 601–609, 2013.
- 272 Dyar, M., Carosino, M., Breves, E., Ozanne, M., Clegg, S., and Wiens, R.: Comparison of partial least
273 squares and lasso regression techniques as applied to laser-induced breakdown spectroscopy of geological
274 samples, *Spectrochimica Acta Part B: Atomic Spectroscopy*, 70, 51–67, 2012.
- 275 Ferreira, E. C., Milori, D. M., Ferreira, E. J., Da Silva, R. M., and Martin-Neto, L.: Artificial neural network
276 for Cu quantitative determination in soil using a portable laser induced breakdown spectroscopy system,
277 *Spectrochimica Acta Part B: Atomic Spectroscopy*, 63, 1216–1220, 2008.
- 278 Fisher, B. T., Johnsen, H. A., Buckley, S. G., and Hahn, D. W.: Temporal gating for the optimization of
279 laser-induced breakdown spectroscopy detection and analysis of toxic metals, *Applied Spectroscopy*, 55,
280 1312–1319, 2001.
- 281 Gent, J. F., Koutrakis, P., Belanger, K., Triche, E., Holford, T. R., Bracken, M. B., and Leaderer, B. P.:
282 Symptoms and medication use in children with asthma and traffic-related sources of fine particle pollution,
283 *Environmental health perspectives*, 117, 1168–1174, 2009.
- 284 Gottfried, J. L., De Lucia, F. C., Munson, C. A., and Miziolek, A. W.: Laser-induced breakdown spec-
285 troscopy for detection of explosives residues: a review of recent advances, challenges, and future prospects,
286 *Analytical and bioanalytical chemistry*, 395, 283–300, 2009.
- 287 Hahn, D. W. and Omenetto, N.: Laser-induced breakdown spectroscopy (LIBS), part I: review of basic diag-
288 nostics and plasma–particle interactions: still-challenging issues within the analytical plasma community,
289 *Applied spectroscopy*, 64, 335A–366A, 2010.
- 290 Hahn, D. W. and Omenetto, N.: Laser-induced breakdown spectroscopy (LIBS), part II: review of instru-
291 mental and methodological approaches to material analysis and applications to different fields, *Applied*
292 *spectroscopy*, 66, 347–419, 2012.
- 293 Hermann, J., Axente, E., Pelascini, F., and Craciun, V.: Analysis of Multi-elemental Thin Films via
294 Calibration-Free Laser-Induced Breakdown Spectroscopy, *Analytical chemistry*, 91, 2544–2550, 2019.
- 295 Hu, S., Ribeiro, E. L., Davari, S. A., Tian, M., Mukherjee, D., and Khomami, B.: Hybrid nanocompos-
296 ites of nanostructured Co₃O₄ interfaced with reduced/nitrogen-doped graphene oxides for selective
297 improvements in electrocatalytic and/or supercapacitive properties, *Rsc Advances*, 7, 33 166–33 176, 2017.
- 298 Hunter, A. J., Morency, J. R., Senior, C. L., Davis, S. J., and Fraser, M. E.: Continuous emissions monitoring
299 using spark-induced breakdown spectroscopy, *Journal of the Air & Waste Management Association*, 50,
300 111–117, 2000.
- 301 Kiefer, J., Tröger, J. W., Li, Z., Seeger, T., Alden, M., and Leipertz, A.: Laser-induced breakdown flame
302 thermometry, *Combustion and flame*, 159, 3576–3582, 2012.
- 303 Kotzagianni, M., Yuan, R., Mastorakos, E., and Couris, S.: Laser-induced breakdown spectroscopy measure-
304 ments of mean mixture fraction in turbulent methane flames with a novel calibration scheme, *Combustion*
305 *and Flame*, 167, 72–85, 2016.

- 306 Martin, M. Z., Labbé, N., André, N., Harris, R., Ebinger, M., Wullschleger, S. D., and Vass, A. A.: High res-
307 olution applications of laser-induced breakdown spectroscopy for environmental and forensic applications,
308 *Spectrochimica Acta Part B: Atomic Spectroscopy*, 62, 1426–1432, 2007.
- 309 Matsumoto, A., Tamura, A., Honda, T., Hirota, T., Kobayashi, K., Katakura, S., Nishi, N., Amano, K.-i.,
310 Fukami, K., and Sakka, T.: Transfer of the species dissolved in a liquid into laser ablation plasma: an
311 approach using emission spectroscopy, *The Journal of Physical Chemistry C*, 119, 26 506–26 511, 2015a.
- 312 Matsumoto, A., Tamura, A., Koda, R., Fukami, K., Ogata, Y. H., Nishi, N., Thornton, B., and Sakka,
313 T.: On-site quantitative elemental analysis of metal ions in aqueous solutions by underwater laser-induced
314 breakdown spectroscopy combined with electrodeposition under controlled potential, *Analytical chemistry*,
315 87, 1655–1661, 2015b.
- 316 Matsumoto, A., Tamura, A., Koda, R., Fukami, K., Ogata, Y. H., Nishi, N., Thornton, B., and Sakka,
317 T.: A calibration-free approach for on-site multi-element analysis of metal ions in aqueous solutions by
318 electrodeposition-assisted underwater laser-induced breakdown spectroscopy, *Spectrochimica Acta Part B:
319 Atomic Spectroscopy*, 118, 45–55, 2016.
- 320 Mukherjee, D. and Cheng, M.-D.: Characterization of carbon-containing aerosolized drugs using laser-
321 induced breakdown spectroscopy, *Applied spectroscopy*, 62, 554–562, 2008a.
- 322 Mukherjee, D. and Cheng, M.-D.: Quantitative analysis of carbonaceous aerosols using laser-induced break-
323 down spectroscopy: a study on mass loading induced plasma matrix effects, *Journal of Analytical Atomic
324 Spectrometry*, 23, 119–128, 2008b.
- 325 Pope III, C. A., Burnett, R. T., Thun, M. J., Calle, E. E., Krewski, D., Ito, K., and Thurston, G. D.: Lung
326 cancer, cardiopulmonary mortality, and long-term exposure to fine particulate air pollution, *Jama*, 287,
327 1132–1141, 2002.
- 328 Rovelli, S., Nischkauer, W., Cavallo, D. M., and Limbeck, A.: Multi-element analysis of size-segregated fine
329 and ultrafine particulate via Laser Ablation-Inductively Coupled Plasma-Mass Spectrometry, *Analytica
330 chimica acta*, 1043, 11–19, 2018.
- 331 Sacks, R. D. and Walters, J. P.: Short-time, spatially-resolved radiation processes in a high-voltage spark
332 discharge, *Analytical Chemistry*, 42, 61–84, 1970.
- 333 Shepherd, J. E., Krok, J. C., and Lee, J. J.: Spark ignition energy measurements in *Jet A*, 2000.
- 334 St-Onge, L., Kwong, E., Sabsabi, M., and Vadas, E.: Quantitative analysis of pharmaceutical products by
335 laser-induced breakdown spectroscopy, *Spectrochimica Acta Part B: Atomic Spectroscopy*, 57, 1131–1140,
336 2002.
- 337 Van Meel, K., Smekens, A., Behets, M., Kazandjian, P., and Van Grieken, R.: Determination of platinum,
338 palladium, and rhodium in automotive catalysts using high-energy secondary target X-ray fluorescence
339 spectrometry, *Analytical chemistry*, 79, 6383–6389, 2007.
- 340 Venecek, M. A., Zhao, Y., Mojica, J., McDade, C. E., Green, P. G., Kleeman, M. J., and Wexler, A. S.:
341 Characterization of the 8-stage Rotating Drum Impactor under low concentration conditions, *Journal of
342 Aerosol Science*, 100, 140–154, 2016.
- 343 Vincze, L., Somogyi, A., Osan, J., Vekemans, B., Török, S., Janssens, K., and Adams, F.: Quantitative trace
344 element analysis of individual fly ash particles by means of X-ray microfluorescence, *Analytical chemistry*,
345 74, 1128–1135, 2002.
- 346 Walters, J.: Historical advances in spark emission spectroscopy, *Applied spectroscopy*, 23, 317–331, 1969.
- 347 Walters, J. P.: Spark discharge: Application multielement spectrochemical analysis, *Science*, 198, 787–797,
348 1977.

- 349 Yao, S., Xu, J., Zhang, L., Zhao, J., and Lu, Z.: Optimizing critical parameters for the directly measurement
350 of particle flow with PF-SIBS, *Scientific reports*, 8, 1868, 2018.
- 351 Zanobetti, A., Franklin, M., Koutrakis, P., and Schwartz, J.: Fine particulate air pollution and its compo-
352 nents in association with cause-specific emergency admissions, *Environmental Health*, 8, 58, 2009.
- 353 Zheng, L., Kulkarni, P., Zavvos, K., Liang, H., Birch, M. E., and Dionysiou, D. D.: Characterization of an
354 aerosol microconcentrator for analysis using microscale optical spectroscopies, *Journal of aerosol science*,
355 104, 66–78, 2017.
- 356 Zheng, L., Kulkarni, P., and Dionysiou, D. D.: Calibration approaches for the measurement of aerosol mul-
357 tielemental concentration using spark emission spectroscopy, *Journal of Analytical Atomic Spectrometry*,
358 33, 404–412, 2018a.
- 359 Zheng, L., Kulkarni, P., and Diwakar, P.: Spatial and temporal dynamics of a pulsed spark microplasma
360 used for aerosol analysis, *Spectrochimica Acta Part B: Atomic Spectroscopy*, 144, 55–62, 2018b.